Unveiling the Activity and Mechanism Alterations by Pyrene Decoration on a Co(II) Macrocyclic Catalyst for CO_2 Reduction

Weilu Zhang,[#a] Hai-Hua Huang,[#b] Zhi-Mei Luo,[c] Fan Ma,[c] Sergio Gonell,[d] Zhuofeng Ke,[b] Liang Tan *[a] Jia-Wei Wang,*[c]*

[a]Key Laboratory of Chemical Biology and Traditional Chinese Medicine Research (Ministry of Education of China), College of Chemistry and Chemical Engineering, Hunan Normal University, Changsha 410081, China

[b]School of Materials Science and Engineering, Sun Yat-sen University, Guangzhou 510275, China.

[c]School of Chemical Engineering and Technology, Sun Yat-sen University, Zhuhai 519082, China.

[d]Institute of Advanced Materials (INAM), Universitat Jaume I, Av. Vicente Sos Baynat s/n., Castelló 12006, Spain.

#Weilu Zhang and Hai-Hua Huang contributed equally to this work.

*Correspondence: Zhuofeng Ke: kezhf3@mail.sysu.edu.cn; Liang Tan: liangtan@hunnu.edu.cn; Jia-Wei Wang: wangjw25@mail2.sysu.edu.cn

KEYWORDS. CO_2 reduction; Molecular catalysis; Pyrene decoration; Spectroelectrochemistry; Catalytic mechanism

ABSTRACT: Mechanistic studies involving characterization of crucial intermediates are desirable for rational optimization of molecular catalysts toward CO_2 reduction, while fundamental challenges are associated with such studies. Herein we present the systematic mechanistic investigations on a pyrene-appended Co^{II} macrocyclic catalyst in comparison with its pyrene-free prototype. The comparative results also verify the reasons of the higher catalytic activity of the pyrene-tethered catalyst in noble-metal-free CO_2 photoreduction with various photosensitizers, where a remarkable apparent quantum yield of 36±3% at 425 nm can be obtained for selective CO production. Electrochemical and spectroelectrochemical studies in conjunction with DFT calculations between the two catalysts have characterized the key CO-bound intermediates and revealed their different CO-binding behavior, demonstrating that the pyrene group endows the corresponding Co^{II} catalyst a lower catalytic potential, a higher stability, and a greater ease in CO release, all of which contribute to its better performance.

Introduction

CO_2 reduction has been viewed as a versatile reaction for both relieving the global warming and providing carbon-neutral, renewable fuels.[1-2] Molecular catalysis utilizing transition metal complexes is promising to address efficiency and selectivity issues in CO_2 reduction; their well-defined structures facilitate the optimization of their catalytic performances by means of

identification of catalytic intermediates and determination of their operative mechanisms.[3-4] The molecular catalysts based on earth-abundant metals are relatively appealing for their merits in lowering the expense for large-scale applications.[5-6] Researchers have devoted to tailoring the earth-abundant molecular catalysts for CO_2 reduction with diverse strategies, such as electronic modification,[7-10] extension of conjugation,[8,11] introduction of pendant proton relays,[12-13] Coulombic interaction,[14-15] dinuclear synergy,[16-17] etc. However, the current mechanistic understanding of these effects is challenging and insufficient, especially if experimental and theoretical studies are not well combined, which should be essential in further catalyst optimization.

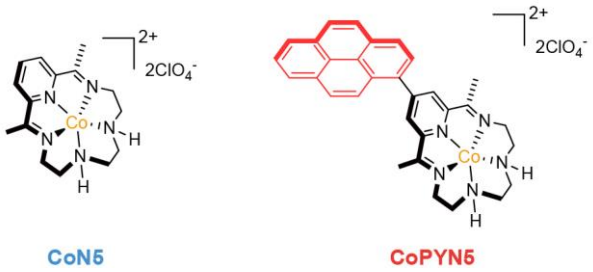

Figure 1. Chemical structures of **CoN5** and **CoPYN5**.

The Co^{II} complexes coordinated by penta-aza-macrocycles containing a pyridyldiimine redox-active moiety and polyamine donors have been employed as excellent molecular catalysts for photocatalytic CO_2 reduction. The first study was contributed by Robert and Lau,[18] reporting $[Co^{II}(\mathbf{N5})](ClO_4)_2$ (**CoN5**; **N5** = (2*E*,12*E*)-2,13-dimethyl-3,6,9,12-tetraaza-1(2,6)-pyridinacyclotri-decaph-ane-2,12-diene; Figure 1) as a high-performance molecular catalyst to achieve a high selectivity of 97% and a turnover number (TON) of 270 for light-stimulated CO_2-to-CO conversion with an Ir^{III} photosensitizer (PS). Then some of us modified **CoN5** by decorating a pyrenyl group at the para position of the pyridyl module, giving

$[Co^{II}(\mathbf{PYN5})](ClO_4)_2$ (**CoPYN5**; **PYN5** = (2*E*,12*E*)-2,13-dimethyl-14-(pyren-1-yl)-3,6,9,12-tetraaza-1(2,6)-pyridinacyclotridecaphane-2,12-diene; Figure 1). **CoPYN5** has exhibited much improved activity and selectivity over the parent **CoN5** in parallel photocatalytic CO_2 reduction to CO.[19-21] More interestingly, the dangling pyrenyl group of **CoPYN5** has allowed CH-π interactions with polymeric carbon nitride[19] or diverse π-π interactions with pyrene-appended Ir^{III} [20] or Cu^{I} [21] PSs, enabling rapid electron communications with these highly conjugated PSs and thus much improved performances toward CO_2 photoreduction. However, the origins of the enhanced intrinsic activity of **CoPYN5** over **CoN5** by pyrene decoration, as well as the catalytic mechanism of **CoPYN5** itself, both remain elusive, which indeed merits detailed investigations for further rational design of this catalyst family or similar prototypes. Herein, we prove the improved catalytic performance of **CoPYN5** relative to **CoN5** with various PSs in noble-metal-free CO_2 photoreduction, and we have combined a systematic electrochemical/spectroelectrochemical (SEC) study with density functional theory (DFT) calculations, where the key intermediates have been characterized and their catalytic mechanisms have been comparatively analyzed. These results highlight the versatile role of the additional pyrenyl group of **CoPYN5** in improving its intrinsic catalytic activity.

Results and Discussion

Photocatalysis. We constructed noble-metal-free photocatalytic systems for CO_2 reduction to compare the catalytic performances between **CoN5** and **CoPYN5** by utilizing either **Al-PS** (Figure 1A) or **Cu-PS** (Figure 1B) as the PS. The photocatalytic data are summarized in Table 1. Visible-light-induced CO_2 reduction was conducted in CH_3CN containing 1,3-dimethyl-2-phenyl-2,3-dihydro-1H-benzo[*d*]imidazole (BIH) as the sacrificial electron donor, triethylamine

(TEA) as the deprotonation agent for the oxidized BIH[21] and 2,2,2-trifluoroethanol (TFE) as the suitable proton source[19] (see Supporting Information (SI) for details). In the photocatalytic systems with either PS, **CoPYN5** exhibits significantly higher activity and selectivity than **CoN5** for CO_2-to-CO conversion. Under nearly parallel conditions, the one with **Cu-PS** is much more active than that with **Al-PS** (ca. 4 times of CO yield) in shorter reaction time, partially due to its much longer-lived excited state (~300 vs. ~10 ns) of **Cu-PS**[21] over that of **Al-PS**.[22] The optimal apparent quantum yield (Φ) for CO formation of 36±3% at 425 nm was thus attained in the system containing **Cu-PS** and **CoPYN5**, over three times of the one with **CoN5** instead (11±1%), which is comparable to many pioneering noble-metal-free molecular systems.[23-26] Therefore, by using two different PSs, we could confirm the markedly enhanced catalytic performances in CO_2 photoreduction by the pyrene decoration on the Co(II) macrocycle.

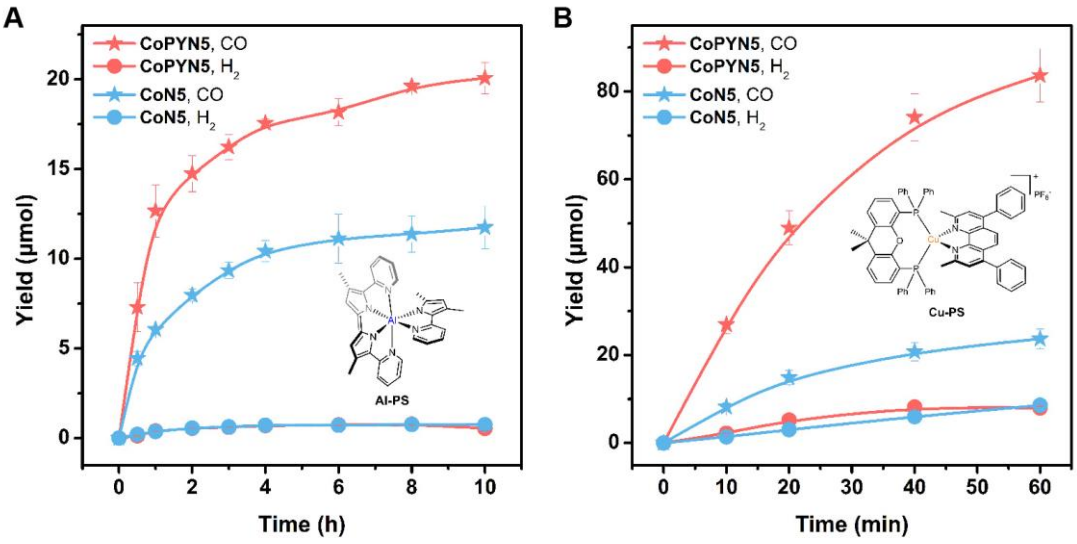

Figure 2. Time Profiles of CO (star) and H_2 (circle) evolution with 50 μM of **CoPYN5** (red traces) or **CoN5** (blue traces) by using 0.50 mM (A) **Al-PS** or (B) **Cu-PS** under 425 nm irradiation. Other conditions are indicated in the SI. Insets in (A) and (B) display the chemical structures of (A) **Al-PS** and (B) **Cu-PS**. The errors represent the standard deviations of three independent measurements.

Table 1. Results of photocatalytic CO_2 reduction.[a]

Entry	PS	Catalyst	n(CO) (μmol)	n(H_2) (μmol)	CO%	TON[d]	Φ(CO)
1[b]	**Al-PS**	**CoPYN5**	20.1±0.9	0.5±0.1	97.6	100±4	3.3±0.6%
2[b]	**Al-PS**	**CoN5**	11.7±1.2	0.8±0.1	93.6	58±6	2.0±0.2%
3[c]	**Cu-PS**	**CoPYN5**	83.7±6.1	8.0±0.3	91.3	418±30	36±3%
4[c]	**Cu-PS**	**CoN5**	23.7±1.0	8.6±0.5	73.4	118±5	11±1%

[a] Standard conditions are indicated in the SI. The errors represent the standard deviations of three independent measurements.

[b] Reaction time = 10 h with Φ determined at 0.5 h.

[c] Reaction time = 1 h with Φ determined at 10 min.

[d] Calculated by the evolved CO (mol) versus the used catalyst (mol).

Electrochemistry. To preliminarily verify the origin of their different activity, cyclic voltammetry was used to investigate the redox properties of **CoPYN5** in comparison with **CoN5** in CH_3CN solutions containing 0.1 M $^nBu_4NPF_6$. The redox potentials (Table 2) are calibrated by ferrocene as the internal reference and converted to vs. NHE (= normal hydrogen electrode) unless otherwise stated. The formal oxidation states are noted and the involvement of ligand-centered reductions will be verified in the subsequent discussion with DFT calculations. First, the cyclic voltammograms (CVs) of **CoPYN5** under Ar show three redox couples at -0.63, -1.31 and -1.46 V (Figure 3A and Table 2). The second reduction wave became more reversible at faster scan rates, while the first and third ones remained irreversible in nature according to their large peak-to-peak separations which increased at faster scan rates (Figure S1), suggesting significant structural changes at these events.[27]

Table 2. Redox potentials.[a]

Catalyst	Atmosphere	E_1 (V)	E_2 (V)	E_3 (V)
CoPYN5	Ar	-0.63	-1.31	-1.46
CoPYN5	CO	-0.65	-1.11	-1.41
CoN5	Ar	-0.66	-1.35	-1.62
CoN5	CO	-0.65	-1.11	-1.43

[a] Determined by the half-wave potentials from the CVs of 1.0 mM catalyst in dry CH_3CN at a scan rate of 0.10 V s^{-1} with scanning potentials incorporating three reduction waves. Potentials are versus NHE.

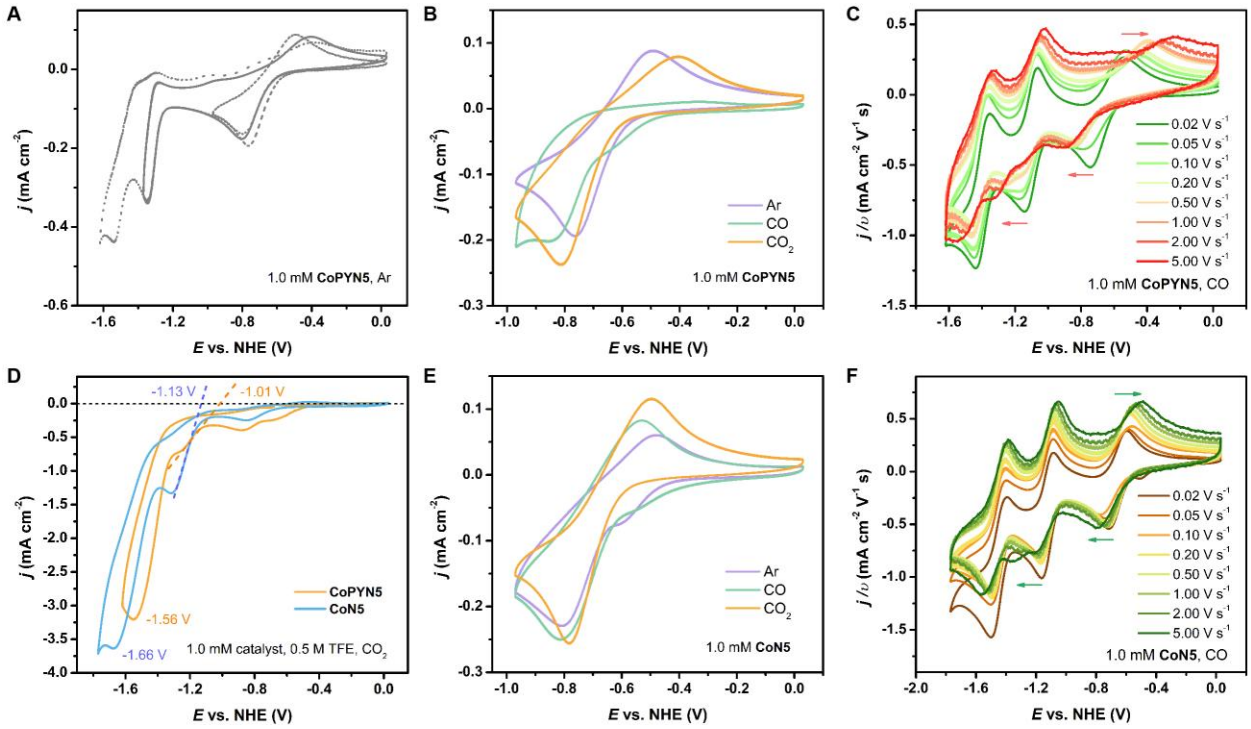

Figure 3. (A) CVs of 1.0 mM **CoPYN5** under Ar with different scanning potential windows. (B,E) CVs of 1.0 mM (B) **CoPYN5** or (E) **CoN5** under Ar (violet), CO (green) and CO_2 (orange), highlighting the first reduction events. (C,F) Scan-rate-normalized CVs of 1.0 mM (C) **CoPYN5** or (F) **CoN5** under CO at varying scan rates from 0.02 to 5.00 V s^{-1}. (D) CVs of 1.0 mM **CoPYN5** (orange) and **CoN5** (blue) under CO_2 with 0.5 M TFE. Scan rate is 0.10 V s^{-1} unless otherwise stated.

Because CO is the main product in the photocatalytic reduction of CO_2, the CVs of **CoPYN5** under CO were collected to investigate the CO binding/dissociation steps (Figure 2C and S3). The introduction of CO firstly eliminated the returning oxidative wave of the first redox couple when scanned up to -1.0 V, while this couple resumed quasi-reversible upon scanning through the three reduction waves (Figure 2B and S2), which suggests the instable binding of CO at this redox event. Its peak-to-peak separation became increasingly larger at increasing scan rates, while its reduction potential is similar to and even slightly more negative the one under Ar (-0.65 vs. -0.63 V; Table 2), indicating the mildly endothermic nature of CO binding at Co(I) species. Additionally, it can be noticed that the scan-rate-normalized redox currents and the potentials both showed negligible changes at higher scan rates (> 0.05 V s^{-1}; Figure 2C), suggesting the lethargic kinetics of the CO-binding chemical step where the main event is attributable to the similar $Co^{II/I}$ reduction event to the one under Ar. The above observations all suggest the rather weak CO binding at the formal Co^{I} state.

For the second redox couple, a notable positive shift by 0.20 V (Table 2) was induced by the presence of 1 atm CO, suggesting a strong CO binding at the formal Co^{0} species. At slow scan rates (< 0.10 V s^{-1}), no substantial shift on this couple was induced by varying the scan rates, indicative of dominant Co^{I}(**PYN5**)(CO)/Co^{0}(**PYN5**)(CO) process. When the scan rate increased to 0.10 V s^{-1} or above, an additional reduction wave emerged at more negative potentials; it shifted to more negative potentials and became more intense at higher scan rates, while the previous reduction wave gradually disappeared. Considering the slow CO binding at the Co^{I} state, as well as the fact that the reduction potential of the newly emerged wave is similar to the one under Ar, the reduction events along with increasing scan rates can be described as transitions from Co^{I}(**PYN5**)(CO)/Co^{0}(**PYN5**)(CO) to Co^{I}(**PYN5**)/Co^{0}(**PYN5**)(CO) and then to

bare $Co^{I/0}$ reduction. The third redox couple is highly reversible at varying scan rates with a slightly shifted redox potential under CO versus the one under argon (-1.41 vs. -1.46 V), suggesting Co^{0}(**PYN5**)(CO)/Co^{-1}(**PYN5**)(CO) or Co^{0}(**PYN5**)(CO)/Co^{-1}(**PYN5**) process, which will be confirmed by subsequent SEC studies.

When the atmosphere was changed to CO_2, the first redox wave did not show obvious change with maintaining the oxidation wave, implying the absence of CO_2 binding at this reduction event (Figure 3B). A current enhancement peaking at -1.26 V suggests the catalytic CO_2 reduction (Figure S4A), and a further catalytic wave appeared at -1.56 V with addition of 0.5 M TFE as the proton source (Figure 3D and S4B).

The parallel CVs of **CoN5** under argon, in contrast, exhibit three successive redox couples at more negative potentials, namely -0.66, -1.35 and -1.62 V (Figure S5). The overall positive shifts indicate the electron-withdrawing effects of the pyrenyl group in **CoPYN5**. We noticed that the redox waves of **CoN5** under argon became ill-mannered when the potentials were scanned to the third reduction wave at moderate scan rate (< 0.50 V s^{-1}), implying the decomposition of **CoN5** at this reduction event and a lower stability than **CoPYN5**, which also complicates the illustration of its redox behavior. More importantly, several differences were discovered in comparing the CO binding behavior between **CoPYN5** and **CoN5**. Firstly, the first redox couple of **CoN5** under CO remained reversible in different scanning windows and scan rates (Figure 3E, 3F, S6 and S7), suggesting a less favored CO-binding kinetics at its formal Co^{I} state than that of **CoPYN5** (Figure 3B). Secondly, a larger positive shift of $Co^{I/0}$ reduction wave under CO was observed in the CV of **CoN5** than that of **CoPYN5** (0.24 vs. 0.20 V, Table 2), indicating a stronger CO binding at the Co^{0} state of **CoN5**. Thirdly, the third redox couple of **CoN5** is much positively shifted under CO compared to the one under Ar (-1.43 vs. -1.62 V; Table 2), also

indicative of a much stronger CO binding at this reduction event than that of **CoPYN5**, which also implies a more significant CO poisoning behavior at its triply reduced species. Besides these disparities, the scan-rate-dependent CVs of **CoN5** under CO (Figure 3F and S7) are similar to those of **CoPYN5** with analogous kinetic conclusions.

In the presence of identical [TFE] and CO_2 (Figure 2D and Figure S8), a larger catalytic wave could be observed in the CV of **CoN5** than that of **CoPYN5** (ca. -3.7 vs. -3.2 mA cm^{-2}), while the required potentials are more negative, including both onset[9] (at -1.13 vs. -1.01 V) and peaking (at -1.66 vs. -1.56 V) potentials. These observations further suggest the scaling relation[28] between catalytic activity and overpotential upon the introduction of pyrene group which apparently acts as an electron-withdrawing substituent. However, the low overpotential can be a more important parameter for catalyst functioning in CO_2 photoreduction when the driving force from the PS is fixed, manifesting the more favorable photocatalysis with **CoPYN5**. We need to note that the foot-of-the-wave[29] or peak current[8] analysis is not applicable to compare their electrocatalytic activities because of the lack of well-defined redox couples under catalysis-free conditions. Bulk electrolysis were also not employed in this work to compare their activity which were previously conducted for **CoPYN5**[19] or **CoN5,**[18] due to their moderate performances and decomposition under long-term electrochemical operations.

UV-vis-SEC. To shed light on the catalytic intermediates involved in the CO_2 reduction, UV-vis spectroelectrochemistry (UV-vis-SEC) within an optically transparent thin-layer electrode (OTTLE) cell was utilized in both cases of **CoPYN5** and **CoN5** in dry CH_3CN (Figure 4 and S9-S12). Initially under Ar during the first reduction event, the UV-vis absorbance of **CoPYN5** showed a small decrease in the region below ca. 400 nm, along with a slight increase at the shoulder of the previous Co^{II} *d-d* transition band tailing until ca. 700 nm (Figure S9A),

suggesting the $Co^{II/I}$ reduction. During the second reduction up to -1.4 V (vs. NHE), the above shoulder continued to be intensified, affording an absorption band at 530 nm, along with a small absorption enhancement at the region below 400 nm (Figure S9B), forming the formal Co^0 species. Further reduction of this species down to -1.6 V induced the emergence of a structured absorption band peaking at 508 and 573 nm, indicative of a formal Co^{-1} intermediate (Figure S9C).

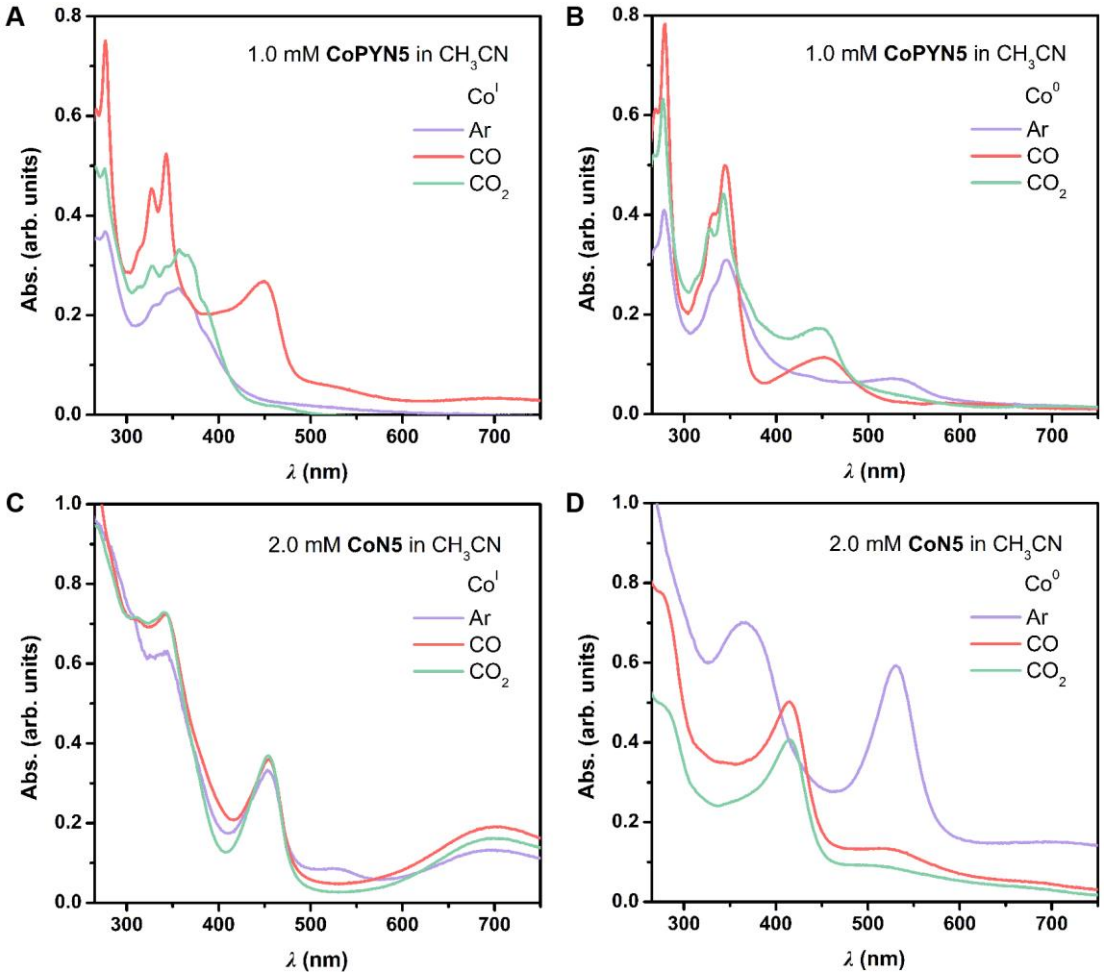

Figure 4. UV-vis-SEC. UV-vis spectra in CH_3CN with (A,B) 1.0 mM **CoPYN5** at (A) Co^I and (B) Co^0, or (C,D) 2.0 mM **CoN5** at (C) Co^I and (D) Co^0, under Ar (violet), CO (red) and CO_2 (green).

Under CO atmosphere, in sharp contrast, we observed different spectra from those under Ar during the UV-vis-SEC experiments. At the first reduction, several absorption bands at 288, 326, 344 and 448 nm appeared with a broad absorption above 470 nm (Figure S10A). At the more negative potential (up to -1.4 V; Figure S10B), the band at 449 nm gradually decreased with a small red shift to 452 nm, concomitant with a slightly increased absorption centered at ca. 625 nm. Both of the two above species are different from the ones under Ar at identical potentials (Figure 4A), suggesting the significant CO binding at the formal Co^{I} and Co^{0} species in the time scale of UV-vis-SEC, respectively. Notably, further reduction up to -1.6 V enabled the formation of a spectral species similar to the one under Ar, both exhibiting the structured absorption band at 508 and 573 nm (Figure S7C and S10C), confirming the Co^{0}(**PYN5**)(CO)/Co^{-1}(**PYN5**) is the preferred event. The above results are in good agreement with the CO binding behavior suggested by the CV results (Figure 4C and S3).

Finally, under CO_2, the first reduction induced the generation of UV-vis absorption spectra similar to the ones under Ar (Figure 4A and S11A), which manifests the formation of Co^{I} species with no CO_2 binding, consistent with the CV results (Figure 4B). Then the second reduction afforded an absorption spectrum reminiscent of either of the formal Co^{I} and Co^{0} intermediates under CO (Figure 4B and S11B). Between them, the one for Co^{0}(CO) species seems to be more similar for both the absent band at around 700 nm, suggesting its emergence under CO_2. This observation also indicates the CO_2 reduction to CO catalyzed by **CoPYN5** taking place at the second reduction wave. In the absence of proton source, a reductive disproportion mechanism[8] will proceed: $2CO_2 = CO + CO_3^{2-}$. However, further reduction caused a continuously decreasing absorbance (Figure S11C), manifesting its decomposition at this reduction potential in the absence of proton source.

We also operated the UV-vis-SEC studies on **CoN5** under parallel studies (Figure 4C, 4D and S12). We noticed that the third reduction of **CoN5** induced overall decreased absorption under all atmospheres, indicative of complex decomposition at this reduction event. We therefore mainly investigated the first and second reduction events of **CoN5** in UV-vis-SEC. Also consistent with the CV results, the UV-vis spectra of **CoN5** at formal Co^{I} state are identical under three kinds of atmosphere (Figure 4C), showing no substrate binding, especially no CO binding, taking place with the Co^{I} species of **CoN5**, showing the slow kinetics of CO binding to its Co^{I} center. This in turn suggests that the CO binding is more kinetically favored for **CoPYN5** at its the Co^{I} state. This trend seems counterintuitive as the more electron-rich Co center in **CoN5** should favor the CO binding processes.[30] An alternate explanation is that the local CO concentration can be improved by the *n*-π* interactions[31] between CO molecules and the pyrene group in **CoPYN5** for more kinetically facile CO binding at Co^{I}. Then, analogous CO-bound species at Co^{0} were observed under either CO_2 or CO because of their similar UV-vis spectra (Figure 4D).

FT-IR-SEC. To corroborate the above UV-vis-SEC results and acquire the bonding information of the intermediates, we further implemented the Fourier-transformed infrared SEC (FT-IR-SEC) on **CoPYN5** under either CO_2 or CO atmosphere. Firstly, we conducted the FT-IR-SEC under CO to check the CO-bound species. The formal $Co^{I}(CO)$ species appeared with signal at 1988 cm^{-1} upon the reduction at -0.6~-1.0 V (Figure 5A). By applying more negative potentials at -1.0~-1.6 V, the signal at 1988 cm^{-1} faded while the one at 1894 cm^{-1} intensified, which appeared at -0.8 V, as well as the appearance of another signal at 1817 cm^{-1}, suggesting the consumption of $Co^{I}(CO)$ species along with the formation of $Co^{0}(CO)$ and $Co^{-1}(CO)$ intermediate (Figure 5B). The appearance of multiple CO-bound species can be ascribed to the even longer time scale in

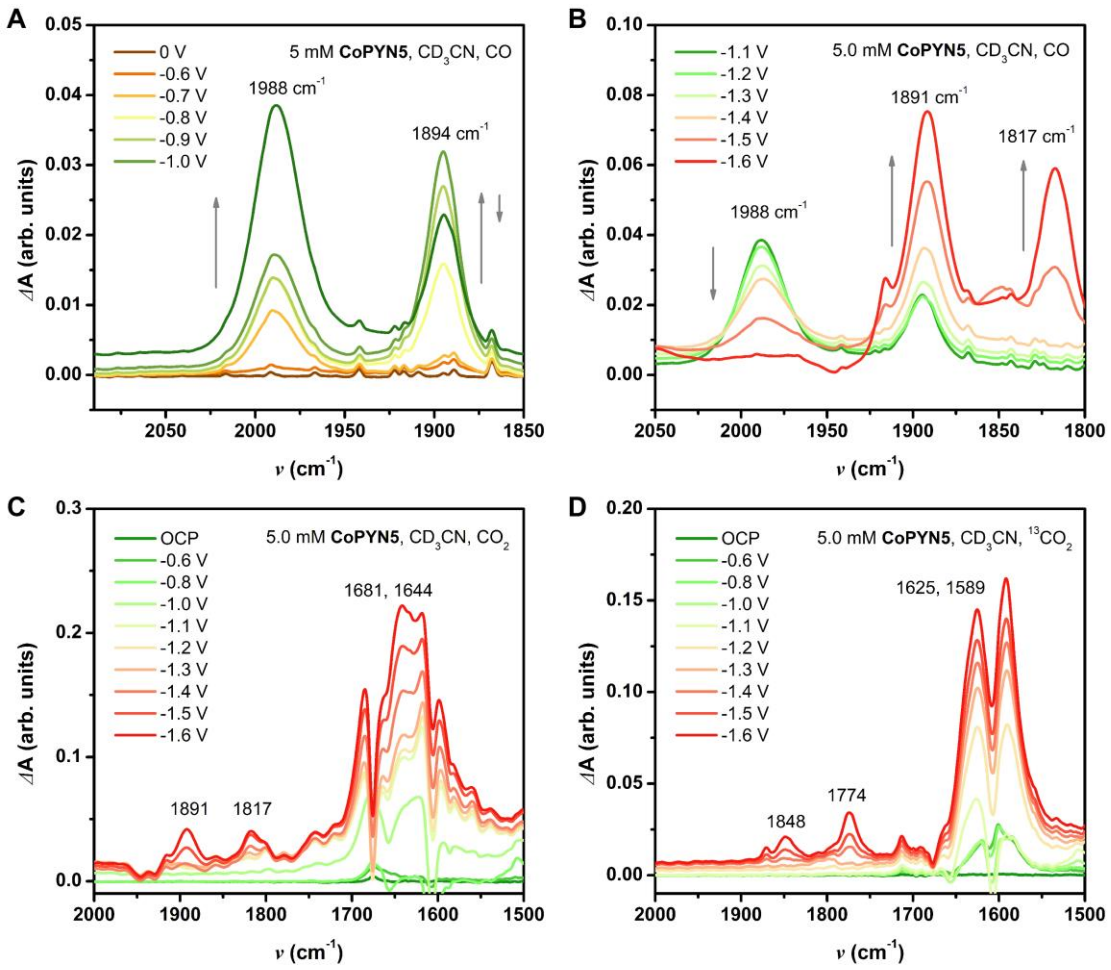

Figure 5. FT-IR-SEC of CoPYN5. Temporal evolution of differential FT-IR spectra of 5.0 mM **CoPYN5** in CD_3CN in an OTTLE cell under (a,b) CO, (c) $^{12}CO_2$ and (d) $^{13}CO_2$.

FT-IR-SEC (> 5 min) compared to UV-vis-SEC (ca. 1 min) measurements (see SI for experimental details). Subsequently, under CO_2 atmosphere, no significant signals appeared until the potentials more negative than -1.0 V were applied, indicating that the spectral changes were induced by the doubly reduced species of **CoPYN5**. In detail, as shown in Figure 5C, the peaks at 1681 and 1644 cm^{-1} can be attributed to the non-coordinated HCO_3^-/CO_3^{2-} species.[32] At more negative potentials up to the third reduction wave of **CoPYN5**, we could notice the appearance of two peaks at 1891 and 1817 cm^{-1}, in good agreement of the CO-bound species at the Co^0 and

Co^{-1} center of **CoPYN5**, as observed by FT-IR-SEC under CO. This observation demonstrates the reductive disproportion of CO_2 to CO and the CO binding processes mediated by **CoPYN5**. To further prove the above attributions, $^{13}CO_2$ was introduced instead of $^{12}CO_2$, where overall shifts of the above-mentioned signals to lower wavenumbers could be observed, indicating that these signals originate from CO_2 and also supporting the above assignments (Figure 5D).[32]

Parallelly, we also conducted the FT-IR-SEC studies on **CoN5** (Figure S13). Under CO, the formal $Co^{I}(CO)$ and $Co^{0}(CO)$ species appeared with C=O signals at 1987 and 1892 cm^{-1} upon the reduction at potentials more negative than -1.2 V (Figure S13A), probably due to the slow kinetics of CO binding to the Co^{I} center. By applying more negative potentials exceeding -1.5 V, the signal at 1987 cm^{-1} disappeared along with the enhanced signal at 1894 cm^{-1}, suggesting the consumption of $Co^{I}(CO)$ intermediate and further formation of formal $Co^{0}(CO)$ species (Figure S13B). The absence of IR signal for the formal $Co^{-1}(CO)$ species may be attributed to the low stability of the triply reduced intermediate from **CoN5**. Then the FT-IR-SEC experiments with **CoN5** under CO_2 (Figure S13C) show the formation of carbonate species at 1675 and 1639 cm^{-1} among the applied potentials at -1.3 ~ -1.8 V. Meanwhile, a sharp peak at 1891 cm^{-1} formed, which is assignable to the $Co^{0}(CO)$ intermediate by referencing the FT-IR-SEC results under CO.

DFT calculation on proposed mechanism. DFT calculation was applied to further investigate the catalytic mechanisms of $[Co\mathbf{L}(CH_3CN)_2]^{2+}$ (**L** refers to **N5** or **PYN5**) in CO_2 reduction to CO. The spin variations on Co have been considered and their optimized energies are shown in Table S1 and S2. The key calculated redox potentials and free energy changes were displayed in Figure 6, with the coordinates of all calculated species are included the Appendix in the SI.

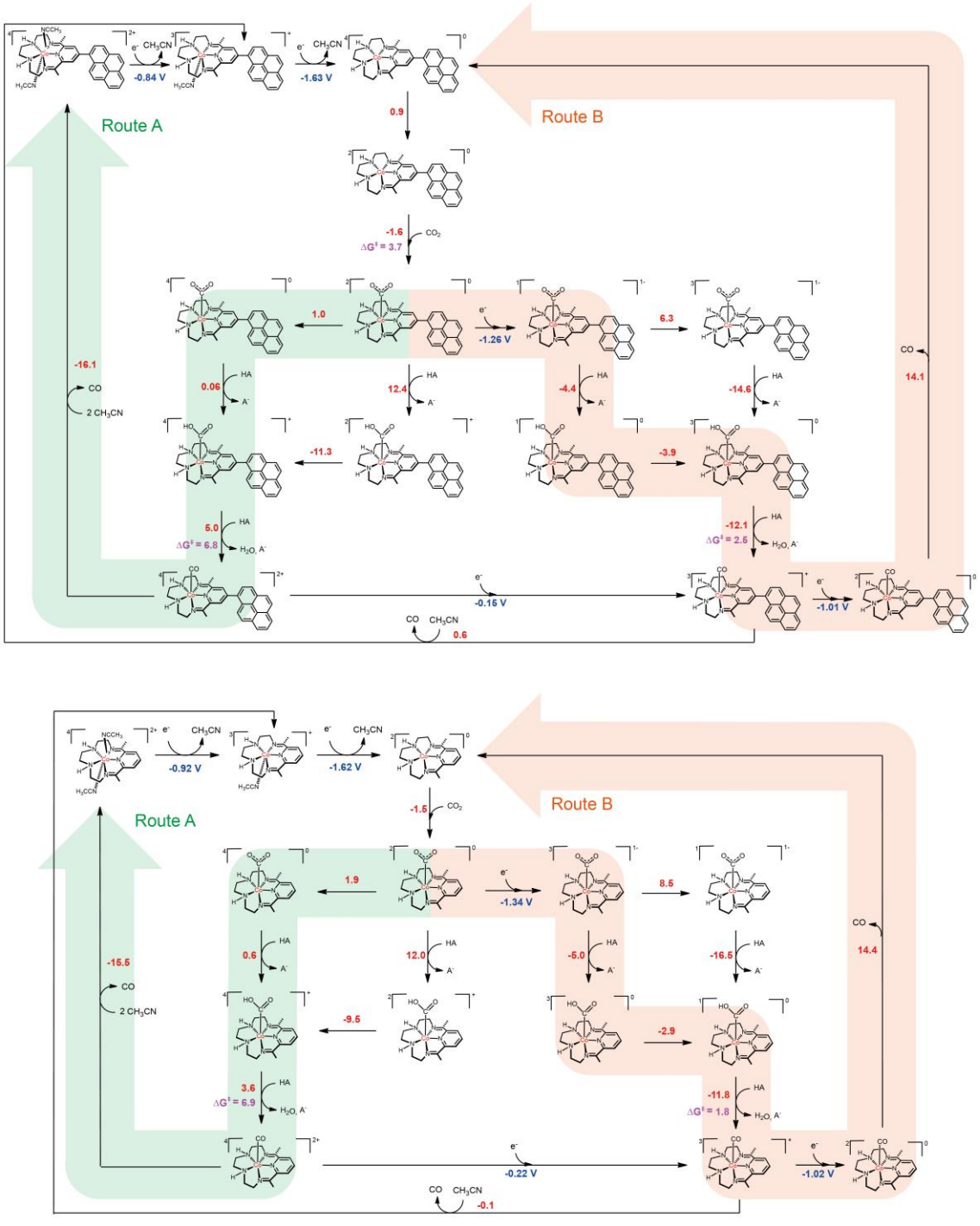

Figure 6. The calculated mechanisms of (upper) **CoPYN5** and (bottom) **CoN5** in catalyzing CO_2 reduction to CO. Spin multiplicities and charges of the intermediates are presented at the upper left and the upper right,

respectively. The free energy changes are presented in red in kcal mol^{-1}. Two viable catalytic routes are highlighted with (A) green and (B) orange arrows.

Initially, the two successive one-electron reduction processes of $[Co\mathbf{L}(CH_3CN)_2]^{2+}$ allow the formation of the reactive species $[Co\mathbf{L}]^0$ for CO_2 binding, accompanied with the loss of two CH_3CN molecules successively. We also examined the atom charge distribution by using atomic dipole moment corrected Hirshfeld (ADCH) population[33-34] (Table S3), displaying the partial electron localization on the redox-active moieties of both ligands, which suggest the involvement of ligand-centered reduction events[18,27] for all the reduced intermediates of both cobalt catalysts. Especially, the pyrenyl group in **CoPYN5** shares the charges upon reduction, showing its ability as electron reservoir. For the spin states of the key Co^0 active species, the quartet species is dominant for $[Co(\mathbf{PYN5})]^0$, while $[Co(\mathbf{N5})]^0$ favors the low-spin doublet state, which can activate and bind CO_2 with no energy barrier, presumably due to its more electron-rich Co^I center (Table S3, Entry 3). With respect to the $[Co(\mathbf{PYN5})]^0$, although an energy barrier of 9.0 kcal mol^{-1} is required for the activation of CO_2 by the dominant quartet species, a lower activation free energy of 3.7 kcal mol^{-1} was calculated for the CO_2 coordination to the low-spin doublet $[Co(\mathbf{PYN5})]^0$ which is accessible from the quartet species with a small free energy change of 1.0 kcal mol^{-1}. After the formation of doublet $[Co\mathbf{L}(CO_2)]^0$ in both cases, it seems that its direct protonation is highly endergonic (12.4 kcal mol^{-1} for **CoPYN5** and 12.0 kcal mol^{-1} for **CoN5**) under photocatalytic conditions (pH = 18.8). However, the corresponding high-spin quartet intermediates, of which formation requires additional free energy changes which are uphill but still accessible (1.0 kcal mol^{-1} for **CoPYN5** and 1.9 kcal mol^{-1} for **CoN5**), are easier to be protonated with small free energy changes of 0.06 kcal mol^{-1} for $[Co(\mathbf{PYN5})(CO_2)]^0$ and 0.6 kcal mol^{-1} for $[Co(\mathbf{N5})(CO_2)]^0$, respectively. Subsequently, the C-O cleavage assisted by the

Bronsted acid (assuming carbonic acid[35]) to form the CO-bound species requires an energy barrier of 6.8 or 6.9 kcal mol^{-1} for $[Co(\mathbf{PYN5})(COOH)]^{+}$ or $[Co(\mathbf{N5})(COOH)]^{+}$, respectively. Finally, CO can be released spontaneously (-16.1 kcal mol^{-1} for $[Co(\mathbf{PYN5})(CO)]^{2+}$ and -15.5 kcal mol^{-1} for $[Co(\mathbf{N5})(CO)]^{2+}$) to regenerate $[Co\mathbf{L}(CH_3CN)_2]^{2+}$, completing the Route A in the proposed mechanism (green traces in Figure 6).

We also considered other pathways where the further reduction of doublet $[Co\mathbf{L}(CO_2)]^{0}$ takes place to avoid the quite endergonic protonation (> 12.0 kcal mol^{-1}) and in turn forms the singlet $[Co\mathbf{L}(CO_2)]^{-}$. The redox potentials were calculated as -1.26 and -1.34 V for the reduction of $[Co(\mathbf{PYN5})(CO_2)]^{0}$ and $[Co(\mathbf{N5})(CO_2)]^{0}$, respectively, which are accessible under photocatalytic conditions (more negative than -1.4 V). Therefore, this reaction pathway can be more favored than the above one by the facile electron transfer energetics, initiating the Route B in the proposed mechanism (orange traces in Figure 6). The subsequent protonation steps become exergonic, with free energy changes of -4.4 and -5.0 kcal mol^{-1} for the formation of $[Co(\mathbf{PYN5})(COOH)]^{0}$ and $[Co(\mathbf{N5})(COOH)]^{0}$, respectively. The generated singlet species can be converted into the high-spin triplet intermediates with lower free energy values (-3.9 kcal mol^{-1} for $[Co(\mathbf{PYN5})(COOH)]^{0}$ and -2.9 kcal mol^{-1} for $[Co(\mathbf{N5})(COOH)]^{0}$). Then $[Co(\mathbf{PYN5})(CO)]^{+}$ and $[Co(\mathbf{N5})(CO)]^{+}$ can be generated after C-O cleavage assisted by carbonic acid with free energy barriers of 2.5 and 1.8 kcal mol^{-1}, respectively. The release of CO and re-coordination by CH_3CN was calculated to be nearly thermoneutral (-0.1 kcal mol^{-1} for $[Co(\mathbf{PYN5})(CO)]^{+}$ and 0.6 kcal mol^{-1} for $[Co(\mathbf{N5})(CO)]^{+}$). It should be noted that $[Co(\mathbf{PYN5})(CO)]^{+}$ and $[Co(\mathbf{N5})(CO)]^{+}$ might undergo spontaneous reduction to form $[Co(\mathbf{PYN5})(CO)]^{0}$ and $[Co(\mathbf{N5})(CO)]^{0}$ since the reduction potentials were calculated to be -1.01 and -1.02 V, respectively, both less negative than the driving forces < -1.4 V. The formation of $[Co\mathbf{L}(CO)]^{0}$ species has been observed in the above

SEC studies under CO_2, indicating this pathway is experimentally supported, while it leads to endergonic, rate-determining steps of CO release (14.1 kcal mol^{-1} for [Co(**PYN5**)(CO)]^0 and 14.4 kcal mol^{-1} for [Co(**N5**)(CO)]^0). The slight thermodynamic ease in the CO-release reaction from calculation is consistent with the less favored CO binding at the Co^0 state of **CoPYN5** than **CoN5**, as experimentally revealed by the smaller positive shift of $Co^{I/0}$ reduction wave under CO in the CV of **CoPYN5** than that of **CoN5** (0.20 vs. 0.24 V, Table 2). Accordingly, the more feasible CO dissociation at Co^0 center could be another reason for the higher activity of **CoPYN5** in photocatalytic CO_2 reduction.

Conclusion

In summary, the catalytic mechanism of **CoPYN5** for CO_2 reduction and the origin of its higher catalytic efficiency over its parent **CoN5** has been systematically elucidated by additional photocatalytic evaluations, electrochemistry, spectroelectrochemistry coupled with UV-vis absorption and FT-IR spectroscopies, as well as DFT calculations. The combined outcome indicates that the lower catalytic potential, higher robustness of the multiply reduced species and more facile CO desorption may contribute to the higher catalytic performance of **CoPYN5**. We believe that this study will provide operative orientations for mechanistic studies and valuable insights for the subtle structural elaborations on the molecular catalysts for CO_2 reduction.

ASSOCIATED CONTENT

Supporting Information.

The following files are available free of charge.

Experimental and computational details, supporting figures and DFT calculation coordinates (PDF)

AUTHOR INFORMATION

Corresponding Author

*Zhuofeng Ke: kezhf3@mail.sysu.edu.cn

*Liang Tan: liangtan@hunnu.edu.cn

*Jia-Wei Wang: wangjw25@mail2.sysu.edu.cn

Author Contributions

Conceptualization: HHH, LT, JWW

Methodology: WLZ, HHH, FM, JWW

Investigation: WLZ, HHH, JWW, FM, ZML, ZK, LT

Visualization: WLZ, HHH, JWW

Supervision: JWW, ZK, LT

Writing—original draft: WLZ, HHH, JWW

Writing—review & editing: WLZ, HHH, SG, ZK, LT, JWW

The manuscript was written through contributions of all authors. All authors have given approval to the final version of the manuscript.

Funding Sources

Guangdong Basic and Applied Basic Research Foundation: 2020A1515110017, 2021A1515012033 and 2022A1515110079

Science and Technology Planning Project of Guangzhou: 202201011113

ACKNOWLEDGMENT

We thank the financial supports from Guangdong Basic and Applied Basic Research Foundation (2020A1515110017, 2021A1515012033 and 2022A1515110079), as well as Science and Technology Planning Project of Guangzhou (202201011113). We also thank the expertise on CO binding kinetics from Prof. Alexander Miller from University of North Carolina at Chapel Hill.

REFERENCES

(1) Zhao, Y.; Liu, Z. Recent Advances in Photocatalytic CO_2 Reduction Using Earth-Abundant Metal Complexes-Derived Photocatalysts. *Chin. J. Chem* . **2018,** *36*, 455-460.

(2) Andrei, V.; Wang, Q.; Uekert, T.; Bhattacharjee, S.; Reisner, E. Solar Panel Technologies for Light-to-Chemical Conversion. *Acc. Chem. Res.* **2022,** *55*, 3376-3386.

(3) Wang, J.-W.; Zhong, D.-C.; Lu, T.-B. Artificial Photosynthesis: Catalytic Water Oxidation and CO_2 Reduction by Dinuclear Non-Noble-Metal Molecular Catalysts. *Coord. Chem. Rev.* **2018,** *377*, 225-236.

(4) Liu, D.-C.; Zhong, D.-C.; Lu, T.-B. Non-Noble Metal-Based Molecular Complexes for CO_2 Reduction: From the Ligand Design Perspective. *EnergyChem* **2020,** *2*, 100034.

(5) Zhang, J.; Zhong, D.; Lu, T. Co(II)-Based Molecular Complexes for Photochemical CO_2 Reduction. *Acta Physico Chimica Sinica* **2020,** *0*, 2008060-2008068.

(6) Wang, J.-W.; Zhang, X.; Velasco, L.; Karnahl, M.; Li, Z.; Luo, Z.-M.; Huang, Y.; Yu, J.; Hu, W.; Zhang, X.; Yamauchi, K.; Sakai, K.; Moonshiram, D.; Ouyang, G. Precious-Metal-Free CO_2 Photoreduction Boosted by Dynamic Coordinative Interaction between Pyridine-Tethered Cu(I) Sensitizers and a Co(II) Catalyst. *JACS Au* **2023**, DOI: 10.1021/jacsau.3c00218, in press.

(7) Costentin, C.; Passard, G.; Robert, M.; Saveant, J. M. Ultraefficient Homogeneous Catalyst for the CO_2-to-CO Electrochemical Conversion. *Proc. Natl. Acad. Sci. U. S. A.* **2014,** *111*, 14990-14994.

(8) Wang, J. W.; Huang, H. H.; Sun, J. K.; Ouyang, T.; Zhong, D. C.; Lu, T. B. Electrocatalytic and Photocatalytic Reduction of CO_2 to CO by Cobalt(II) Tripodal Complexes: Low Overpotentials, High Efficiency and Selectivity. *ChemSusChem* **2018,** *11*, 1025-1031.

(9) Li, Z.; Wang, J.-W.; Huang, Y.; Ouyang, G. Enhancing CO_2 Photoreduction Via the Perfluorination of Co(II) Phthalocyanine Catalysts in a Noble‐Metal‐Free System. *Chin. J. Catal.* **2023,** *49*, 160-167.

(10) Huang, H.-H.; Dai, M.; Liu, L.; Liu, J.; Zhao, C.; Vignesh, A.; Ke, Z. Dual Roles of the Electronic Effect on Selectivity: Pincer Nickel-Electrocatalyzed CO_2 Reduction. *Catal. Sci. Technol.* **2021,** *11*, 874-885.

(11) Thoi, V. S.; Kornienko, N.; Margarit, C. G.; Yang, P.; Chang, C. J. Visible-Light Photoredox Catalysis: Selective Reduction of Carbon Dioxide to Carbon Monoxide by a Nickel N-Heterocyclic Carbene-Isoquinoline Complex. *J. Am. Chem. Soc.* **2013,** *135*, 14413-14424.

(12) Ronne, M. H.; Cho, D.; Madsen, M. R.; Jakobsen, J. B.; Eom, S.; Escoude, E.; Hammershoj, H. C. D.; Nielsen, D. U.; Pedersen, S. U.; Baik, M. H.; Skrydstrup, T.; Daasbjerg, K. Ligand-Controlled Product Selectivity in Electrochemical Carbon Dioxide Reduction Using Manganese Bipyridine Catalysts. *J. Am. Chem. Soc.* **2020,** *142*, 4265-4275.

(13) Roy, S. S.; Talukdar, K.; Jurss, J. W. Electro- and Photochemical Reduction of CO_2 by Molecular Manganese Catalysts: Exploring the Positional Effect of Second-Sphere Hydrogen-Bond Donors. *ChemSusChem* **2021,** *14*, 662-670.

(14) Martin, D. J.; Mayer, J. M. Oriented Electrostatic Effects on O_2 and CO_2 Reduction by a

Polycationic Iron Porphyrin. *J. Am. Chem. Soc.* **2021,** *143*, 11423-11434.

(15) Narouz, M. R.; De La Torre, P.; An, L.; Chang, C. J. Multifunctional Charge and Hydrogen-Bond Effects of Second-Sphere Imidazolium Pendants Promote Capture and Electrochemical Reduction of CO_2 in Water Catalyzed by Iron Porphyrins. *Angew. Chem. Int. Ed.* **2022,** *61*, e202207666.

(16) Ouyang, T.; Wang, H.-J.; Huang, H.-H.; Wang, J.-W.; Guo, S.; Liu, W.-J.; Zhong, D.-C.; Lu, T.-B. Dinuclear Metal Synergistic Catalysis Boosts Photochemical CO_2-to-CO Conversion. *Angew. Chem. Int. Ed.* **2018,** *57*, 16480-16485.

(17) Guo, Z.; Chen, G.; Cometto, C.; Ma, B.; Zhao, H.; Groizard, T.; Chen, L.; Fan, H.; Man, W.-L.; Yiu, S.-M.; Lau, K.-C.; Lau, T.-C.; Robert, M. Selectivity Control of CO Versus $HCOO^-$ Production in the Visible-Light-Driven Catalytic Reduction of CO_2 with Two Cooperative Metal Sites. *Nat. Catal.* **2019,** *2*, 801-808.

(18) Chen, L.; Guo, Z.; Wei, X. G.; Gallenkamp, C.; Bonin, J.; Anxolabehere-Mallart, E.; Lau, K. C.; Lau, T. C.; Robert, M. Molecular Catalysis of the Electrochemical and Photochemical Reduction of CO_2 with Earth-Abundant Metal Complexes. Selective Production of CO vs HCOOH by Switching of the Metal Center. *J. Am. Chem. Soc.* **2015,** *137*, 10918-10921.

(19) Wang, J.-W.; Gil-Sepulcre, M.; Huang, H.-H.; Solano, E.; Mu, Y.-F.; Llobet, A.; Ouyang, G. CH-π Interaction Boosts Photocatalytic CO_2 Reduction Activity of a Molecular Cobalt Catalyst Anchored on Carbon Nitride. *Cell Rep. Phys. Sci.* **2021,** *2*, 100681.

(20) Wang, J. W.; Huang, H. H.; Wang, P.; Yang, G.; Kupfer, S.; Huang, Y.; Li, Z.; Ke, Z.; Ouyang, G. Co-Facial π–π Interaction Expedites Sensitizer-to-Catalyst Electron Transfer for High-Performance CO_2 Photoreduction. *JACS Au* **2022,** *2*, 1359-1374.

(21) Wang, J. W.; Li, Z.; Luo, Z. M.; Huang, Y.; Ma, F.; Kupfer, S.; Ouyang, G. Boosting CO_2

Photoreduction by Π-Π-Induced Preassembly between a Cu(I) Sensitizer and a Pyrene-Appended Co(II) Catalyst. *Proc. Natl. Acad. Sci. U. S. A.* **2023,** *120*, e2221219120.

(22) Wang, J. W.; Ma, F.; Jin, T.; He, P.; Luo, Z. M.; Kupfer, S.; Karnahl, M.; Zhao, F.; Xu, Z.; Jin, T.; Lian, T.; Huang, Y. L.; Jiang, L.; Fu, L. Z.; Ouyang, G.; Yi, X. Y. Homoleptic Al(III) Photosensitizers for Durable CO_2 Photoreduction. *J. Am. Chem. Soc.* **2023,** *145*, 676-688.

(23) Takeda, H.; Kamiyama, H.; Okamoto, K.; Irimajiri, M.; Mizutani, T.; Koike, K.; Sekine, A.; Ishitani, O. Highly Efficient and Robust Photocatalytic Systems for CO_2 Reduction Consisting of a Cu(I) Photosensitizer and Mn(I) Catalysts. *J. Am. Chem. Soc.* **2018,** *140*, 17241-17254.

(24) Steinlechner, C.; Roesel, A. F.; Oberem, E.; Päpcke, A.; Rockstroh, N.; Gloaguen, F.; Lochbrunner, S.; Ludwig, R.; Spannenberg, A.; Junge, H.; Francke, R.; Beller, M. Selective Earth-Abundant System for CO_2 Reduction: Comparing Photo- and Electrocatalytic Processes. *ACS Catal.* **2019,** *9*, 2091-2100.

(25) Takeda, H.; Monma, Y.; Ishitani, O. Highly Functional Dinuclear Cu^I-Complex Photosensitizers for Photocatalytic CO_2 Reduction. *ACS Catal.* **2021,** *11*, 11973-11984.

(26) Yuan, H.; Cheng, B.; Lei, J.; Jiang, L.; Han, Z. Promoting Photocatalytic CO_2 Reduction with a Molecular Copper Purpurin Chromophore. *Nat. Commun.* **2021,** *12*, 1835.

(27) Wang, J.-W.; Yamauchi, K.; Huang, H.-H.; Sun, J.-K.; Luo, Z.-M.; Zhong, D.-C.; Lu, T.-B.; Sakai, K. A Molecular Cobalt Hydrogen Evolution Catalyst Showing High Activity and Outstanding Tolerance to CO and O_2. *Angew. Chem. Int. Ed.* **2019,** *58*, 10923-10927.

(28) Azcarate, I.; Costentin, C.; Robert, M.; Saveant, J. M. Through-Space Charge Interaction Substituent Effects in Molecular Catalysis Leading to the Design of the Most Efficient Catalyst of CO_2-to-CO Electrochemical Conversion. *J. Am. Chem. Soc.* **2016,** *138*, 16639-16644.

(29) Costentin, C.; Drouet, S.; Robert, M.; Savéant, J. M. Turnover Numbers, Turnover

Frequencies, and Overpotential in Molecular Catalysis of Electrochemical Reactions. Cyclic Voltammetry and Preparative-Scale Electrolysis. *J. Am. Chem. Soc.* **2012,** *134*, 11235-11242.

(30) Schneider, J.; Jia, H.; Muckerman, J. T.; Fujita, E. Thermodynamics and Kinetics of CO_2, CO, and H^+ Binding to the Metal Centre of CO_2 Reduction Catalysts. *Chem. Soc. Rev.* **2012,** *41*, 2036-2051.

(31) Singh, S. K.; Das, A. The n → π* Interaction: A Rapidly Emerging Non-Covalent Interaction. *PCCP* **2015,** *17*, 9596-9612.

(32) Froehlich, J. D.; Kubiak, C. P. The Homogeneous Reduction of CO_2 by [Ni(Cyclam)](+): Increased Catalytic Rates with the Addition of a CO Scavenger. *J. Am. Chem. Soc.* **2015,** *137*, 3565-3573.

(33) Lu, T.; Chen, F. Atomic Dipole Moment Corrected Hirshfeld Population Method. *J. Theor. Comput. Chem.* **2012,** *11*, 163-183.

(34) Lu, T.; Chen, F. Multiwfn: A Multifunctional Wavefunction Analyzer. *J. Comput. Chem.* **2012,** *33*, 580-592.

(35) Huang, H. H.; Zhang, J. H.; Dai, M.; Liu, L.; Ye, Z.; Liu, J.; Zhong, D. C.; Wang, J. W.; Zhao, C.; Ke, Z. Dual Electronic Effects Achieving a High-Performance Ni(II) Pincer Catalyst for CO_2 Photoreduction in a Noble-Metal-Free System. *Proc. Natl. Acad. Sci. U. S. A.* **2022,** *119*, e2119267119.

SYNOPSIS

The origins of activity improvement and the catalytic mechanisms of a pyrene-appended Co(II) catalyst is clarified by electrochemical and spectroelectrochemical techniques coupled with DFT calculations.